

Continuum and molecular-dynamics simulation of nanodroplet collisionsRaunak Bardia,¹ Zhi Liang,² Pawel Koblinski,² and Mario F. Trujillo^{1,*}¹*Department of Mechanical Engineering, University of Wisconsin-Madison, Madison, Wisconsin 53706, USA*²*Materials Science and Engineering Department, Rensselaer Polytechnic Institute, Troy, New York, 12180, USA*

(Received 23 September 2015; published 9 May 2016)

The extent to which the continuum treatment holds in binary droplet collisions is examined in the present work by using a continuum-based implicit surface capturing strategy (volume-of-fluid coupled to Navier-Stokes) and a molecular dynamics methodology. The droplet pairs are arranged in a head-on-collision configuration with an initial separation distance of 5.3 nm and a velocity of 3 ms⁻¹. The size of droplets ranges from 10–50 nm. Inspecting the results, the collision process can be described as consisting of two periods: a preimpact phase that ends with the initial contact of both droplets, and a postimpact phase characterized by the merging, deformation, and coalescence of the droplets. The largest difference between the continuum and molecular dynamics (MD) predictions is observed in the preimpact period, where the continuum-based viscous and pressure drag forces significantly overestimate the MD predictions. Due to large value of Knudsen number in the gas ($Kn_{\text{gas}} = 1.972$), this behavior is expected. Besides the differences between continuum and MD, it is also observed that the continuum simulations do not converge for the set of grid sizes considered. This is shown to be directly related to the initial velocity profile and the minute size of the nanodroplets. For instance, for micrometer-size droplets, this numerical sensitivity is not an issue. During the postimpact period, both MD and continuum-based simulations are strikingly similar, with only a moderate difference in the peak kinetic energy recorded during the collision process. With values for the Knudsen number in the liquid ($Kn_{\text{liquid}} = 0.01$ for $D = 36\text{nm}$) much closer to the continuum regime, this behavior is expected. The 50 nm droplet case is sufficiently large to be predicted reasonably well with the continuum treatment. However, for droplets smaller than approximately 36 nm, the departure from continuum behavior becomes noticeably pronounced, and becomes drastically different for the 10 nm droplets.

DOI: [10.1103/PhysRevE.93.053104](https://doi.org/10.1103/PhysRevE.93.053104)**I. INTRODUCTION**

Over the last decade or so, significant engineering interest has been focused on time and length scales where the continuum approximations become questionable. Analyses between molecular dynamics (MD) and continuum-level calculations have been performed to study channel flows [1–3] of nanometer dimensions. These studies focused on the departure from continuum-level fluid-wall behavior. Liu and Li [2] concluded that channels with size greater than 150 molecular diameters follow the continuum model with stick boundary conditions, and Gărăjeu et al. [3] incorporated a continuum form of fluid wall interaction, obtaining good agreement with MD results for even smaller channel sizes. One of the key differences observed in some studies has been an increased effective viscosity due to liquid-wall interface in very small channels as compared to the estimates from continuum models [4,5].

For multiphase flow applications, in particular the gas-liquid system, the situation can be even more problematic since the large discrepancy in the respective mass densities of each phase can give rise to situations where the continuum treatment (i.e., application of continuum-level equations) may hold reasonably well in the liquid phase, but not so well in the gas phase. This line of thought is in agreement with Sharp et al. [6], where it is argued that liquids continue to follow the continuum regime for length scales that are about two orders smaller than gaseous flows.

Out of the large variety of configurations in gas-liquid systems, a recurring and common configuration consists of liquid droplets. For instance, a number of studies have considered the coalescence of two micrometer or submicrometer droplets and the dynamics of the resulting jumping droplet [7–10]. The kinetic energy of the jumping droplet comes from the release of surface energy during the coalescence of droplets. This interesting phenomenon has been demonstrated to have a variety of applications in heat pipes [11], thermal diodes [12], self-cleaning surfaces [13], energy harvesting [14], and sintering [15].

The continuum-level binary droplet collision phenomenon has been previously investigated [16–18], where analytical expressions for coalescence efficiency have been developed [19]. Additionally, a detailed description of coalescence regimes has been presented by Qian and Law [20]. However, the literature is very limited for droplets having nanometer scale dimensions. The first systematic investigation for nanoscale binary droplet collision was done by Ming et al. [21], where they concluded that continuum-level droplet collision models are applicable for nanometer-scale argon clusters. Subsequent MD simulations of argon nanodroplet collisions [15,22] report a classification of the collision process according to different regimes established in the continuum-level categorization. Owing to the increased surface-to-volume ratio for these nanodroplets, coalescence is the dominant result of these collisions. Simulations of polymer nanodroplets undergoing head-on collision have also been studied, as reported by Kim [23]. The main goal in his work was to characterize the deformation process and the contact radius evolution, in comparison to the continuum Hertzian model of solid

*mtrujillo@wisc.edu

elastic balls. This contact radius is defined as the radius of the circular cross section representing the contact area between the two merging droplets. With the exception of the early moments during initial contact and extending until the coalescing droplets assume the prolate-ellipsoid shape, the process is well represented by the Hertzian model.

While some knowledge of the nanodroplet collision process has been gained in previous MD simulations, the focus of these works was not directed at understanding and characterizing the departures from continuum behavior that occur with decreasing droplet size. In the present work, this topic is taken by combining MD [24,25] and continuum-level simulations [26] of binary droplet collisions, and by exploring the discrepancies in collision behavior. The systems studied consist of argon droplets undergoing binary head-on collisions with diameters ranging from 10–50 nm. Within this range, significant differences in collision behavior between the continuum and MD treatment are noted. The main reason for choosing argon is that its interatomic potential has a relatively simple form and is adequately represented with Lennard-Jones potential. Furthermore, the reported MD simulations employed 10^6 atoms and are able to simulate the entire droplet collision process within reasonable time. This provides attractive conditions from which to compare to continuum-level simulations.

In what follows, descriptions of the continuum-level simulation and MD approach are given in Sec. II, where the continuum simulation consists of an algebraic volume-of-fluid methodology. The simulation setup is described in Sec. III. A benchmark configuration of droplets having 36 nm diameter (D) is initially compared in Sec. IV between both methods. The discrepancies are then analyzed by considering the numerical sensitivities associated specifically with the continuum and MD approach in Sec. V. In Sec. VI, this comparison is extended by considering independently the role of viscosity and by performing droplet collision calculations with different diameter droplets.

II. NUMERICAL METHODS

A. Volume of fluid

The code used in the present work pertains to an open-source solver (interFoam), which forms part of a larger distribution of computational mechanics solvers and C++ libraries of OpenFOAM[®]. In a relatively recent publication from our group [26], a detailed description of the algorithm is presented along with a systematic verification and validation of the code pertaining to different aspects of two-phase flow behavior. In the current paper, the presentation of the numerical methodology is succinctly described. Following standard procedures for solving fluid mechanics problems under isothermal conditions, only mass and momentum conservation are enforced, i.e., the energy equation is not solved.

In the present case, an incompressible treatment is enforced, i.e., $\nabla \cdot \mathbf{u} = 0$. The first part of the solution consists of the transport of the local liquid fraction, α , which is defined at the computational cell level (Ω_i), i.e.,

$$\alpha(\mathbf{x}_i, t) = \frac{1}{|\Omega_i|} \int_{\Omega_i} \mathbb{I}(\mathbf{x}, t) dV, \quad (1)$$

where \mathbb{I} is a liquid phase indicator function and is defined as one at points occupied by liquid and zero at points where gas is present. The discrete finite volume solution for the transport of α_i (corresponding to cell i) is obtained from

$$\frac{\alpha_i^{n+1} - \alpha_i^n}{\Delta t} = -\frac{1}{|\Omega_i|} \sum_{f \in \partial\Omega_i} (F_u + \lambda_M F_c)^n, \quad (2)$$

where the unsteady term is discretized using forward Euler scheme, and the advection term appears as a summation over the cell faces (f) of Ω_i . Quantities evaluated at the faces are subscripted by f . The advection fluxes F_u and F_c are expressed by

$$F_u = \phi_f \alpha_{f, \text{upwind}} \quad \text{and} \quad (3)$$

$$F_c = \phi_f \alpha_f + \phi_{rf} \alpha_{rf} (1 - \alpha)_{rf} - F_u, \quad (4)$$

where ϕ_f (volume flux) is given by

$$\phi_f = \mathbf{u}_f \cdot \mathbf{S}_f. \quad (5)$$

The role of the delimiter λ_M in Eq. (2) is to separate the numerical treatment given to the evolution of the liquid fraction in the interfacial region as opposed to the single-phase region. Specifically, away from interface or its neighboring cells $\lambda_M = 0$. This gives

$$\frac{\alpha_i^{n+1} - \alpha_i^n}{\Delta t} = -\frac{1}{|\Omega_i|} \sum_{f \in \partial\Omega_i} F_u^n \quad (\lambda_M = 0, \text{ single-phase region}). \quad (6)$$

In this part of the domain, there are no gradients of α and its evolution can be simply obtained by an upwind treatment without any difficulties.

In the interfacial region, Eq. (2) becomes

$$\frac{\alpha_i^{n+1} - \alpha_i^n}{\Delta t} = -\frac{1}{|\Omega_i|} \sum_{f \in \partial\Omega_i} \phi_f \alpha_f + \phi_{rf} \alpha_{rf} (1 - \alpha)_{rf} \quad (\lambda_M = 1, \text{ interfacial region}). \quad (7)$$

As elaborated in our earlier publication [26], the action of the flux on the right-hand side is to mitigate the effects of numerical diffusion that would naturally occur when advecting a field as sharp as a liquid fraction. This is done through the action of a compressive term $[\phi_{rf} \alpha_{rf} (1 - \alpha)_{rf}]$, which is aligned normal to the interface. There are a small fraction of cells, where λ_M varies between 1 and 0. These cells are always located in the interfacial region and are treated with a mixture of upwind and compressive fluxes.

With respect to momentum, the following equation is solved

$$\frac{\partial \rho \mathbf{v}}{\partial t} + \nabla \cdot (\rho \mathbf{v} \otimes \mathbf{v}) = -\nabla p_d + [\nabla \cdot (\mu \nabla \mathbf{v}) + \nabla \mathbf{v} \cdot \nabla \mu] - \mathbf{g} \cdot \mathbf{x} \nabla \rho + \gamma_{lv} \kappa \nabla \alpha, \quad (8)$$

where the continuum surface tension model of Ref. [27] is employed to treat the surface tension force. As is usually done in implicit interface capturing strategies, the density and viscosity fields are computed by

$$\rho = \rho_l \alpha + \rho_g (1 - \alpha) \quad \text{and} \quad \mu = \mu_l \alpha + \mu_g (1 - \alpha). \quad (9)$$

Introducing the following nondimensional quantities, denoted by a superscript *,

$$\begin{aligned} \mathbf{x}^* &= \frac{\mathbf{x}}{D}, & \mathbf{u}^* &= \frac{\mathbf{u}}{V_o}, & P^* &= \frac{P}{\rho_l V_o^2}, & \rho^* &= \frac{\rho}{\rho_l}, \\ \kappa^* &= \kappa D, & t^* &= \frac{V_o}{D} t, & \text{and } \mu^* &= \frac{\mu}{\mu_l}, \end{aligned} \quad (10)$$

into the momentum equation yields,

$$\begin{aligned} &\frac{\partial(\rho^* \mathbf{u}^*)}{\partial t^*} + \nabla^* \cdot (\rho^* \mathbf{u}^* \mathbf{u}^*) \\ &= -\nabla^* P^* + \frac{1}{\text{Re}_L} \{ \nabla^* \cdot [\mu^* \nabla^* (\mathbf{u}^*)] \\ &\quad + \nabla^* (\mathbf{u}^*) \cdot \nabla^* \mu^* \} + \frac{1}{\text{We}_L} \kappa^* (\nabla^* \alpha^*), \end{aligned} \quad (11)$$

where

$$\text{Re}_L = \frac{\rho_l V_o D}{\mu_l} \quad \text{and} \quad \text{We}_L = \frac{\rho_l V_o^2 D}{\gamma_{lv}}. \quad (12)$$

Note that gravitational term of the momentum equation has not been included in Eq. (11). Considering the large value of the Froude number, $(V_o/(\sqrt{Dg}) = 5,048)$, the gravitational force can be safely neglected.

The solution of the momentum equation [Eq. (11)] is obtained via a PISO [28] iteration procedure. The treatment enforces incompressibility. A predictor velocity is first constructed and then corrected to ensure momentum balance and mass continuity. Explicit formulation of the predictor velocity is a two-step process, where first the viscous, advective,

and temporal terms in the momentum equation are used to generate a cell-centered vector field, which is then projected to cell faces using a second-order scheme. Contributions from surface tension and gravity terms are then added, concluding the predictor formulation. This procedure enforces a consistent discretization of surface tension and pressure gradient [26].

With respect to the behavior of the code, we have performed a number of comparisons to other algebraic VoF methods, interface reconstruction VoF schemes, and level set methods [26]. It was found that mass conservation was one of the strongest characteristics of the current algebraic approach. In a three-dimensional (3D) sphere in single vortex test cases, the mass error was $1.303 \times 10^{-7}\%$ for the current code. For the particle level set method [29] and the coupled level set and volume of fluid (CLSVOF) [30], the error was 2.6% and 0.4%, respectively. This level of superior performance is expected from VoF code and does not change much with grid resolution. Perhaps a more telling characteristic concerns standard advection tests. With respect to this category, the current algebraic method is comparable in accuracy to an earlier CLSVOF method [31] and the efficient least-squares volume-of-fluid interface reconstruction algorithm [32]. It is only when the present VoF method is compared to other schemes that involve some higher-order representation of the interface at the subgrid level, that the VoF method does noticeably worse, e.g., [33].

B. Molecular dynamics

A truncated and shifted Lennard-Jones (LJ) 12-6 pair potential is employed in the present work, namely

$$u(r) = \begin{cases} 4\epsilon \left[\left(\frac{\sigma}{r} \right)^{12} - \left(\frac{\sigma}{r} \right)^6 \right] - 4\epsilon \left[\left(\frac{\sigma}{r_{\text{cut}}} \right)^{12} - \left(\frac{\sigma}{r_{\text{cut}}} \right)^6 \right] & \text{if } r < r_{\text{cut}} \\ 0 & \text{if } r \geq r_{\text{cut}}, \end{cases} \quad (13)$$

with parameters $\sigma = 0.341\text{nm}$ and $\epsilon = 10.3\text{meV}$, to describe interatomic forces for Ar-Ar interactions [34]. The cutoff distance is $r_{\text{cut}} = 2.5\sigma$. The long-range corrections of the pressure and potential energy are not considered, as they cannot be applied consistently when multiple phases with widely different densities coexist in the same simulation cell. The velocity Verlet algorithm with a time-step size of 0.006 picoseconds (ps) is used to integrate the equations of motion in all MD simulations [35].

To provide fluid property data to continuum-level simulations, equilibrium MD (EMD) simulations are first performed to determine the saturation pressure, surface tension, density, and viscosity of saturated liquid and vapor of Ar at a temperature of 85 K, which is about 7% higher than the melting temperature of solid Ar. These fluid properties are used as inputs to the VoF equations as described in Sec. II A.

1. MD calculation of fluid properties

One key parameter for continuum-level modeling of droplet collisions is the liquid-vapor surface tension, γ_{lv} . To determine this value, a liquid slab of 2160 Ar atoms is placed in the middle of a simulation box, which has a length of 19.2 nm

and cross section area of 3.84 nm by 3.84 nm. The box size is fixed during the simulation, and periodic boundary conditions (PBCs) are applied in all three directions. The system is equilibrated at 85 K (T_o) for 2000 ps using the Berendsen thermostat [36]. A snapshot of liquid-vapor coexisting phase with two interfaces is shown in Fig. 1(a). After the system reaches thermal equilibrium, the thermostat is turned off and the value of the pressure tensor is monitored in 200 planar bins into which the simulation cell was divided. The surface tension is obtained by using the mechanical definition according to Irving and Kirkwood [37,38]

$$\gamma_{lv} = \frac{1}{2} \int_0^{L_x} [P_N(x) - P_T(x)] dx, \quad (14)$$

where P_N is the pressure normal to the interface and P_T is the tangential pressure. The data collection and averaging spanned over a time period of 14000 ps. The profiles for P_N and P_T are shown in Fig. 1(b). The saturation pressure is the average value of P_N . Using the above described procedure, it is determined that $\gamma_{lv} = 8.16 \pm 0.04 \times 10^{-3} \text{kg s}^{-2}$ and $P_{\text{sat}} = 217443.45 \text{kg m}^{-1} \text{s}^{-2}$.

Another important parameter for continuum-level modeling is the viscosity, μ , of the saturated fluid. The viscosity μ can

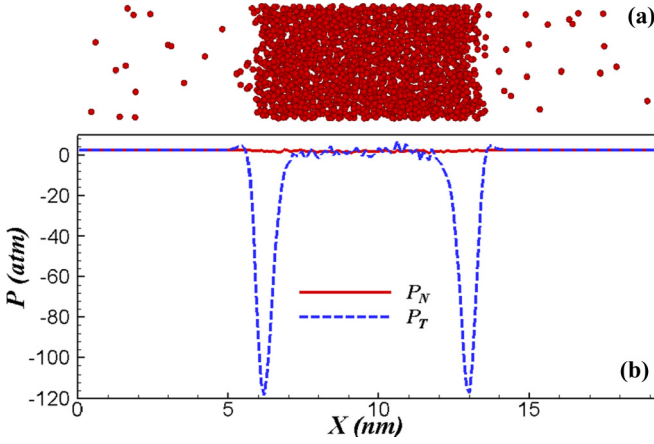


FIG. 1. (a) Snapshot of liquid-vapor coexistent fluid Ar at 85 K. (b) Normal and tangential pressure profile at 85 K.

be determined by the Green-Kubo relation for the shear-stress correlation function in a bulk fluid [39]

$$\mu = \frac{V}{k_B T} \int_0^\infty \langle P_{\alpha\beta}(t) \cdot P_{\alpha\beta}(0) \rangle dt, \quad (15)$$

where

$$P_{\alpha\beta} = \frac{1}{V} \left(\sum_i M v_{i\alpha} v_{i\beta} + \sum_i \sum_{j>i} r_{ij\alpha} f_{ij\beta} \right). \quad (16)$$

In Eqs. (15) and (16), k_B is the Boltzmann constant, V and T are volume and temperature of the system, respectively, P is the pressure tensor, M is the mass of fluid atom, v_i is the translational velocity of the i th molecule, and r and f are interatomic separation and force, respectively. The subscripts α and β denote the vector components, t is the time, and $\langle \dots \rangle$ denotes ensemble average.

To evaluate viscosity of saturated liquid Ar at 85 K, a bulk liquid Ar of 4000 atoms is placed in a cubic simulation box with PBCs applied in three directions and the bulk liquid was equilibrated at P_{sat} and T_o using the Berendsen et al. [36] algorithm with time constants $\tau_T = 0.1\text{ps}$ and $\tau_p = 500\text{ps}$. After the system reaches the desired temperature and pressure, the density of saturated liquid Ar is computed to be $\rho_l = 1.31 \times 10^3 \text{kgm}^{-3}$. Subsequently, the global thermostat and barostat were turned off and the simulation in the microcanonical ensemble is carried out for 10000 ps to determine the shear-stress correlation function. The statistical error associated with the correlation function depends on the total simulation time. As we performed the *NVE* simulation for 10 ns, the statistical error is less than 1%. In some cases, one needs to perform the simulation for thousands of nanoseconds to get good statistics. In our particular case, it was only necessary to have one *NVE* simulation for 10 ns to obtain acceptable statistics. Once the correlation function was obtained, Simpson's rule was used for the time integration to obtain viscosity. As shown in Fig. 2,

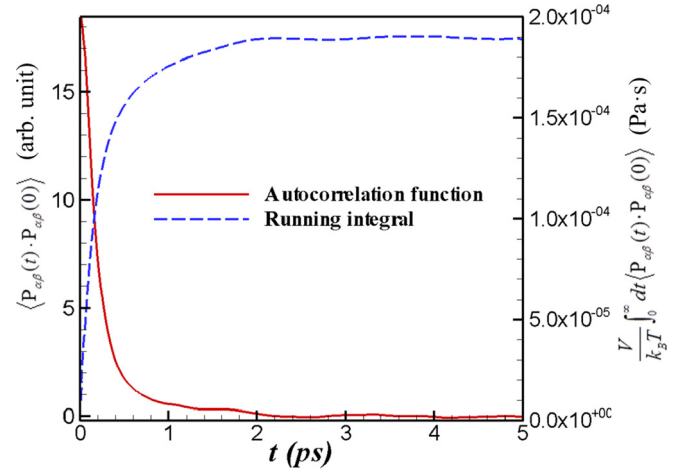


FIG. 2. The shear-stress correlation function and running integral of the correlation function of saturated liquid Ar at 85 K.

the viscosity $\mu_l = 190 \pm 1 \times 10^{-6} \text{kgm}^{-1} \text{s}^{-1}$ is determined from the plateau of the running integral of the correlation function. Using the same method, the density and viscosity of saturated vapor Ar are obtained to be $\rho_v = 13 \text{kgm}^{-3}$ and $\mu_v = 7 \pm 0.1 \times 10^{-6} \text{kgm}^{-1} \text{s}^{-1}$. The calculated fluid properties of Ar at 85 K are summarized in Table I.

III. COLLISION SIMULATION SETUP

This section presents the parameters and setup employed in both methodologies for the benchmark case of droplets having $D = 36\text{nm}$. The system under consideration is initialized with two identical argon droplets in a saturated argon environment with a given initial velocity of V_o (i.e., relative velocity between them is $2V_o$). The system parameters employed in both MD and VoF simulations are listed in Table II in both dimensional and nondimensional form along with the key nondimensional numbers. Length, time, and velocity scales used in the nondimensionalization are given in Eq. (10).

A. Continuum model

The properties for both liquid and vapor phase are obtained from Table I computed in the previous section. The velocity field at all points within the droplets is initially assigned a velocity magnitude of V_o . Similarly, for all points excluding the liquid droplet region the velocity magnitude is initialized to zero. The initial configuration of the system is shown in Fig. 3, where the interdroplet distance is $L_g (= 5.3\text{nm})$.

The computational domain as shown in Fig. 3 is defined with periodic boundary conditions in the direction of initial velocity of the droplets, and wall conditions are imposed on the remaining sides of the domain.

TABLE I. Fluid properties of Ar at 85 K determined from EMD simulations.

$P_{\text{sat}}(\text{kgm}^{-1} \text{s}^{-2})$	$\gamma_{lv}(\text{kgs}^{-2})$	$\rho_l(\text{kgm}^{-3})$	$\mu_l(\text{kgm}^{-1} \text{s}^{-1})$	$\rho_v(\text{kgm}^{-3})$	$\mu_v(\text{kgm}^{-1} \text{s}^{-1})$
2.17×10^5	$8.16 \pm 0.04 \times 10^{-3}$	1310	$190 \pm 1 \times 10^{-6}$	13	$7.0 \pm 0.1 \times 10^{-6}$

TABLE II. Benchmark parameters employed in the MD and continuum VoF simulations in dimensional and (nondimensional*) form.

Parameters	Values (nondimensionalized)
Interdroplet spacing, L_g (L_g^*)	5.3 nm (0.1472)
Diameter of droplet, D (D^*)	36 nm (1)
Initial droplet velocity, V_o (V_o^*)	3 ms^{-1} (1)
Liquid Reynolds number, Re_L	0.745
Liquid Weber number, We_L	0.052

B. MD model

Similarly, the setup is mimicked for MD calculations. To generate an Ar droplet, a [100]-orientated perfect FCC crystal Ar with the lattice constant of 0.54 nm is placed in the center of a big simulation box [see Fig. 4(a)]. The crystal Ar contains 50 unit cells in each of the x , y , and z directions. The size of the simulation box is much greater than that of the Ar crystal. It is 41.3 nm long in the x direction and 56.6 nm long in each of the y and z directions. The PBCs are applied in three directions and the box size is fixed during the simulation.

Using the Berendsen thermostat [36], the system is equilibrated at a temperature of 85 K, which is naturally the same temperature at which the EMD calculations were performed (see section Sec. II B 1). The original crystal Ar soon melted and partially vaporized to establish a liquid-vapor coexisting phase in the simulation box. To distinguish the liquid and vapor phases in the simulation, an Ar atom is defined as liquid if its potential energy is lower than half of that in a saturated bulk liquid at 85 K. This half-value cutoff for phase determination is arbitrary but faithfully reflects the physical transition occurring in the interfacial region. Additionally, the method of distinguishing the phase based on potential energy has a lower computational cost than the density criterion and avoids the undesirable dependency on the size of the

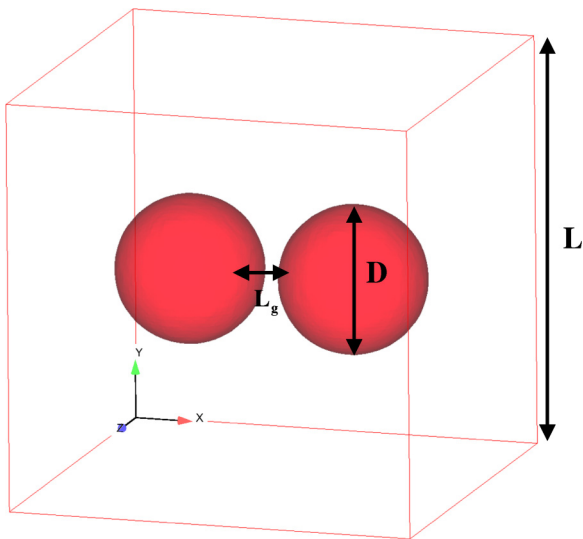


FIG. 3. Initial setup of droplets for continuum simulation. L is the domain size and L_g is the initial separation distance between the two droplets.

subdomain needed for density calculation. It has also been successfully used in study of coalescence of nanoscale droplets on a solid surface [40]. After 2000 ps, the system reaches a steady state and a spherical-shaped liquid Ar droplet is formed in the center of the simulation box. As shown in Fig. 4(b), the diameter of the droplet is around 36 nm and the rest of the space in the simulation box is filled with saturated Ar vapor at 85 K.

To study the collision of two droplets using MD simulations, the liquid-vapor coexisting phase in the simulation box is duplicated in the x direction to create two identical liquid Ar droplets. The new system contains 10^6 Ar atoms and the separation between the two Ar droplets is L_g [see Fig. 4(c)]. To make the two droplets collide, an x -direction velocity of $\pm 3 \text{ ms}^{-1}$ is assigned to liquid atoms in the left and right half of the simulation box respectively and constant- NVE simulations are carried out for a time period of 6000 ps.

IV. INITIAL COMPARISON

Using the benchmark parameters defined in Sec. III A for the continuum approach, and those described in Sec. III B for MD, an initial comparison between both methods is performed. To aid in the selection of a suitable metric for describing the collision process, results from a continuum simulation are depicted in Fig. 5 in terms of liquid bulk kinetic and surface energy. The surface energy trend displays a monotonic decrease from the two droplet configuration to a single coalesced droplet. However, the kinetic energy, defined as,

$$E_{VoF}^{\text{kin}} = \int_{\Omega: \alpha \geq \alpha_{\text{threshold}}} \frac{1}{2} \rho u^2 dV, \quad (17)$$

shows a much more interesting trend characterizing the different stages during the collision process. Here Ω represents the entire domain and the integration is computed over the cells where the liquid phase volume fraction is greater than or equal to a threshold value. For the cases pertinent to this problem, a threshold value of 0.1 provides adequate answers, i.e., having a lower positive threshold leads to very similar values, since the gas phase density is so much lower than the liquid one.

As shown in Fig. 5, as the droplets approach each other, they begin to decelerate due to the build up of the pressure in between them and the viscous drag; consequently, the kinetic energy decreases. Once contact has been made, the surface tension force accelerates the merger of the droplets into a coalesced drop. This process is marked by an increase in kinetic energy reaching a maximum value at approximately $t = 2.5 \text{ ns}$ and a decrease in surface energy. At this stage the liquid is in the form of a tubularlike structure. This is followed by a subsequent decrease in kinetic energy as the droplet reaches a stable configuration aided in part by viscous forces. A small oscillation at around 4.2 ns marks the final part in this process. Due to the more descriptive characterization of collision afforded by the kinetic energy, it is used as a metric of comparison between MD and continuum simulations in the calculations presented in this paper.

In MD, the cylindrical symmetry of the problem is exploited to compute liquid kinetic energy as shown in Fig. 6. The intent is to capture the macroscopic local fluid velocity in droplets

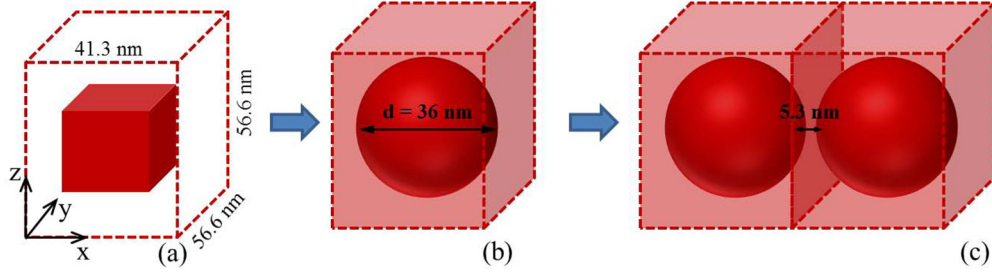


FIG. 4. Schematic diagram of the procedure for generation of two droplets: (a) a cubic Ar crystal in the center of a big simulation box; (b) a liquid Ar droplet surrounded by its saturated vapor; and (c) two identical droplets created by duplication of the simulation box in the x direction.

and not the microscopic thermal velocity. It is determined by averaging velocities of atoms in bins with the width of 2 nm along the axis of cylinder (the axis connecting the center of mass of two droplets) and 2 nm along the radius of cylinder. In each bin the axial velocity, V_x , and radial velocity, V_r , are determined by,

$$V_x = \frac{1}{N} \sum_{i=1}^N v_{x,i}, \quad \text{and} \quad V_r = \frac{1}{N} \sum_{i=1}^N (v_{y,i} \cos \theta + v_{z,i} \sin \theta), \quad (18)$$

where $v_{x,i}$, $v_{y,i}$, $v_{z,i}$ are respectively the x , y , and z component of velocity of atom i in the bin, N is the number of atoms in the bin, the summations are over all liquid atoms in the bin, and θ is the azimuth angle as shown in Fig. 6. Accordingly, the kinetic energy of liquid in each bin is given by

$$E_{MD}^{\text{kin}}(x, r) = \frac{1}{2} \rho_l \pi \left[\left(r + \frac{\Delta r}{2} \right)^2 - \left(r - \frac{\Delta r}{2} \right)^2 \right] \times \Delta x (V_x^2 + V_r^2). \quad (19)$$

The total kinetic energy of the liquid phase is the summation of $E_{MD}^{\text{kin}}(x, r)$ in all bins.

The results with both approaches are shown in Fig. 7 in terms of kinetic energy time histories, with added images to

illustrate the configuration during the impact process. The results clearly show that the peak kinetic energy as well as the time at which it is recorded is noticeably different for both methods. For MD, the peak occurs sooner and is larger than the corresponding results from the continuum simulations. This difference can be identified in the early stages of the collision process, when the droplets have still not made contact. During this time, continuum predictions show a markedly smaller kinetic energy time history. This seems to indicate that the forces causing this deceleration are much larger in continuum level simulations than in MD. This phenomena is examined more carefully in Sec. V.

Although a fraction of the difference in these plots can be attributed to the thermal noise captured in MD simulations, the difference during this initial stage is too large to be completely absorbed by this thermal noise component. This thermal noise originates from the finite number of atoms in each bin, which implies that the local bin average is not exactly the true average. This effect is clearly manifested at the end of collision when the two droplets merge to form a stable bigger droplet and all macroscopic kinetic energy is dissipated to thermal energy. In this case, the continuum-level simulation predicts zero kinetic energy, but the MD simulation still predicts a constant and finite kinetic energy due to the thermal noise. However, this remaining quantity is relatively very small in comparison to the difference between MD and continuum predictions, and thus cannot explain the deviation from continuum behavior.

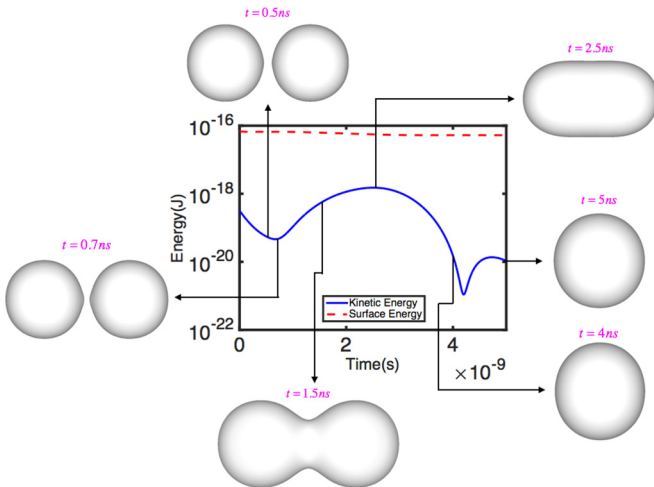


FIG. 5. Continuum simulation log-linear plot for kinetic energy and surface energy for a case of droplet diameter $D = 36$ nm and $\Delta t = 1$ ps.

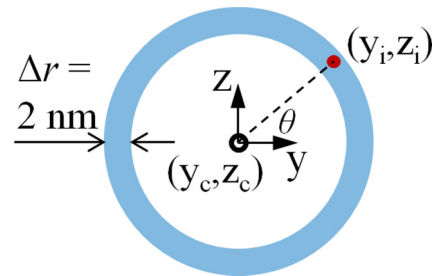


FIG. 6. The schematic diagram of a typical bin used for velocity and kinetic energy calculations. The projection of the bin in the y - z plane has a ring shape with the difference between inner radius and outer radius of 2 nm. The thickness of the bin in the x direction is 2 nm. $(y_c = 28.3$ nm, $z_c = 28.3$ nm) indicates the center of the ring. y_i and z_i are, respectively, y and z coordinate of atom i . θ is the azimuth angle of atom i .

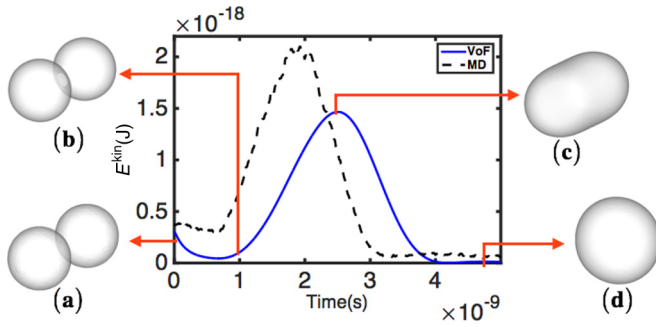


FIG. 7. Kinetic energy plots populated with droplet images at salient points of the process.

As opposed to continuum modeling approaches, e.g., different turbulence treatments, where model parameters influence the results of the simulations to a significant degree, the Navier-Stokes equation is solved directly in the present VoF approach. There are no modeling parameters that can be used to manipulate the results. The only place left to look concerns the numerical parameters, specifically the spatial and temporal resolution. These are systematically examined in the next section.

V. NUMERICAL SENSITIVITIES

A. Continuum VoF model

The main continuum model numerical parameters that will have a direct influence on the simulation of collision dynamics are: (i) domain size, (ii) grid cell size, and (iii) time-step size. These are investigated by independently varying each parameter from their respective benchmark values listed in Table III.

1. Extent of physical domain

The proximity of the boundary can sometimes be responsible for anomalous behavior. In continuum simulations of the type presented here, the boundary needs to be far enough away that it has an inconsequential effect on the dynamics. Testing this plan, the collision process is recalculated using different values for the extent of this domain as illustrated in Fig. 8. All other numerical parameters as delineated in Table III are left unchanged. From the results shown in Fig. 9, it is clearly confirmed that the present physical extent of the domain bears practically no influence on the kinetic energy time history. This parameter cannot explain the difference between MD and VoF simulations.

TABLE III. Benchmark values for the dimensional (nondimensional*) simulation parameters used in continuum VoF simulations.

Parameters	Values
Domain length, $L(L^*)$	100 nm (2.778)
Grid cell size, $\Delta x(\Delta x^*)$	1 nm (0.02778)
Time-step size, $\Delta t(\Delta t^*)$	1 ps (8.33×10^{-5})

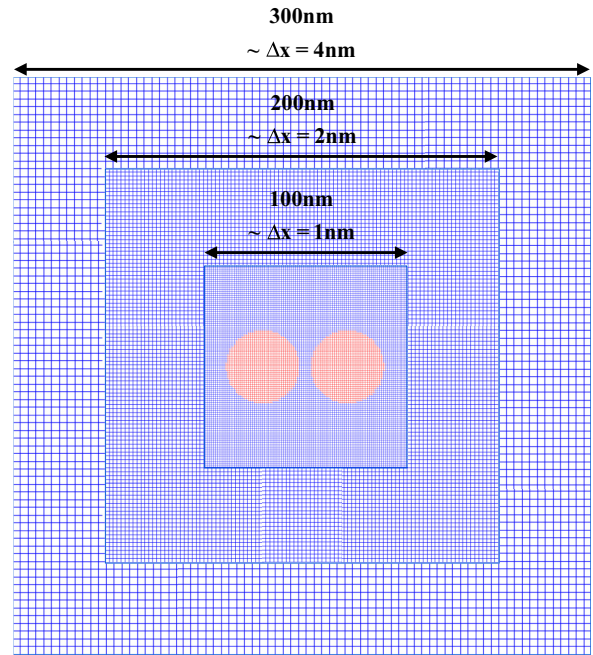


FIG. 8. Extent of the physical domain used in VoF simulations.

2. Time-step size

The collision process is computed at different levels of temporal resolution, namely $\Delta t = 1\text{ps}$, 0.5ps , 0.25ps , and 0.05ps , or respectively in nondimensional form as $\Delta t^* = 83.3 \times 10^{-6}$, 41.7×10^{-6} , 20.8×10^{-6} , and 4.2×10^{-6} . All of the other numerical parameters retain their nominal values as given in Table III. With values for Δt^* that are much lower than one, it is expected that the dynamics are well resolved. A more pertinent metric concerns the potential introduction of numerical noise due purely through spurious interfacial currents [27]. These currents are the result of natural imperfections in the prediction of interfacial curvature that lead to erroneous surface tension forces. As elaborated by Brackbill et al. [27] and generalized by Galusinski and Vigneaux [41],

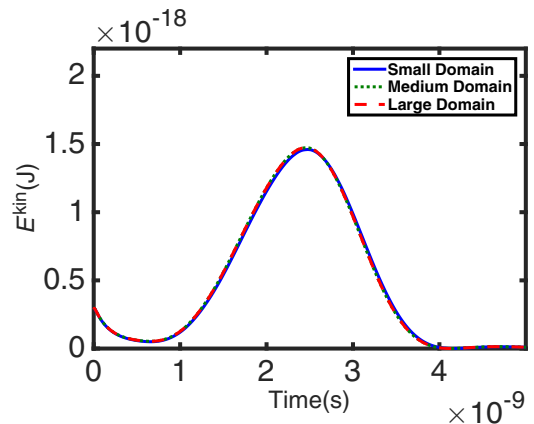


FIG. 9. Kinetic energy time histories for droplet collision simulations employing different domain sizes as depicted in Fig. 8.

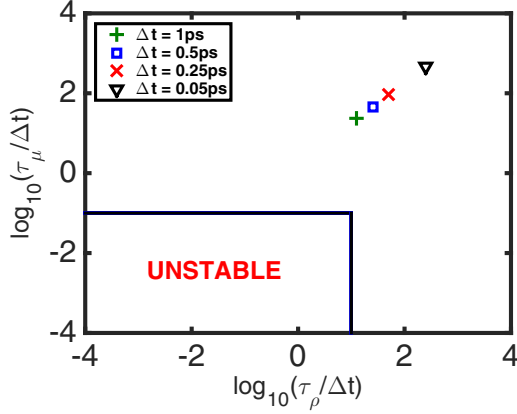


FIG. 10. Regime map denoting regions of numerical instability pertaining to spurious surface tension forces [26].

one way to avoid this problem is to restrict the time-step size below a specified threshold.

For the solver employed in the present work, (INTERFOAM), the spurious flow regime has been previously tested for droplets immersed in a gaseous field [26]. This unstable regime is delineated by the introduction of two time scales [41], namely,

$$\tau_\rho = \sqrt{\frac{\rho_l \Delta x^3}{\gamma_v}} \quad \text{and} \quad \tau_\mu = \frac{\mu_l \Delta x}{\gamma_v}. \quad (20)$$

The respective values for $\tau_\rho/\Delta t$ and $\tau_\mu/\Delta t$ corresponding to the computations previously mentioned are plotted in a regime shown in Fig. 10. Clearly all computations are located well into the stable region. The associated kinetic energy time traces are shown in Fig. 11, which reflect a very weak dependence on Δt . Additionally, these time histories are smooth and do not manifest any of the signs of spurious interface motion. A marginal increase is observed in the maximum kinetic energy of the droplet and the plot shifts slightly towards the right as time-step size decreases. However, the overall dynamics is largely insensitive to reasonable changes in time-step size. Again, this parameter is not responsible for the observed differences between MD and continuum-level simulations.

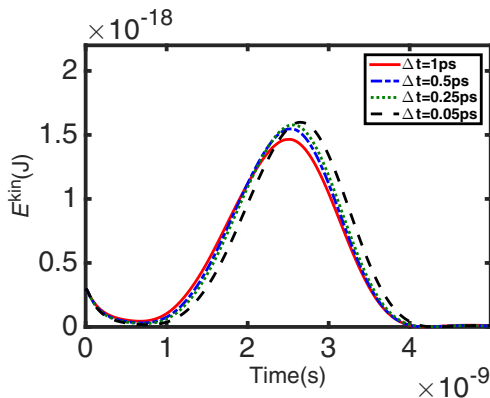


FIG. 11. Kinetic energy variation for droplet collisions with different time-step size.

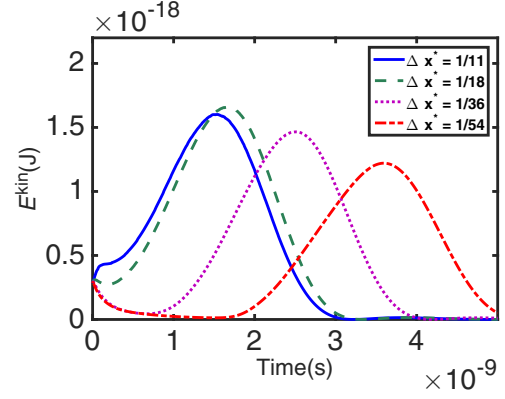


FIG. 12. Kinetic energy time histories for different values of Δx^* .

3. Grid size sensitivity

The calculations performed under the nominal conditions listed in Table III are repeated, but with a grid resolution corresponding to $\Delta x = 3.33\text{nm}$, 2nm , 1nm , 0.667nm or respectively $\Delta x^* = 0.0926$, 0.05556 , 0.02778 , 0.01852 . The results are shown in terms of kinetic energy histories in Fig. 12. It is clear from these plots that the simulations are heavily dependent on the mesh refinement. For the case with $\Delta x^* = 0.0926$, the coarseness of the grid causes the interdroplet spacing (L_g) to remain largely unresolved, which results in an immediate collision between the droplets as compared to other continuum cases, where they decelerate before collision.

To explore the situation, the equation of motion for a single droplet in the limit of small Reynolds number is considered. In our particular case, Re_L does not fall exactly in this limit. Yet, Re_L is sufficiently small such that the Stokes flow treatment is a good approximation as indicated by the drag coefficient versus Reynolds number chart given in Ref. [42].

For a droplet immersed in a gaseous flow, the drag term corresponds to the Hadamard-Rybcynski drag law [43], where the Stokes drag coefficient ($C_{D,\text{Stokes}}$) incorporates a correction to account for the tangential movement of the gas-liquid interface. This is given by

$$C_D = C_{D,\text{Stokes}} \left(\frac{1 + \frac{2}{3}\bar{\mu}}{1 + \bar{\mu}} \right), \quad (21)$$

where

$$\bar{\mu} = \frac{\mu_v}{\mu_l} = \frac{7 \times 10^{-6} \text{kgm}^{-1} \text{s}^{-1}}{190 \times 10^{-6} \text{kgm}^{-1} \text{s}^{-1}} = 0.037 \ll 1. \quad (22)$$

From the corresponding values listed in Table I, $\bar{\mu} = 0.037$, which is much less than one. Hence, to a good approximation, the dynamics can be treated as pertaining to a solid particle moving through a gaseous medium. This gives

$$\frac{d}{dt} \left(\rho_l \frac{4}{3} \pi R^3 V \right) = -6\pi \mu_v R V. \quad (23)$$

As described previously in Sec. III, the velocity field is initialized by assigning a magnitude of V_o at all computational nodes occupied by the droplets, and a magnitude of zero at nodes occupied by gas. As the numerical resolution increases,

the distance between nodes (Δx) decreases accordingly. This has important consequences in the interfacial region of the droplet, where the velocity magnitude changes from V_o to zero over a distance given by $A_1 \Delta x$ [A_1 is a $\mathcal{O}(1)$ constant, generally ranging between 2 and 3]. The implication is that the viscous drag force, which is directly related to the velocity gradient through $\mu(\nabla \mathbf{u} + \nabla \mathbf{u}^T)$ also increases as the numerical resolution improves.

To incorporate this effect, the equation of motion [Eq. (23)] is modified by replacing the drag term with a term that directly accounts for the grid-resolution-dependent viscous force. This yields,

$$\frac{d}{dt} \left(\rho_l \frac{4}{3} \pi R^3 V \right) = -(4\pi R^2) \mu_v \frac{V}{\Delta x}. \quad (24)$$

It is understood that this approximation does not exactly reflect the velocity gradient at every point on the droplet surface or for all time. Rather than striving for a more exact route, which will render the situation too complicated to solve analytically, the motivation here is to arrive at a modeling treatment for the grid sensitivity effect that will explain the results observed in Fig. 12. (The more exact route consisting of full two-phase flow simulations in three dimensions is already being reported in Fig. 12, and does not provide the needed explanation.)

Proceeding with Eq. (24), it is expected that the viscous drag effect will change over time, for instance in a manner similar to Stokes first problem. This term can be treated by an effective drag term, specifically $\mu_v \frac{V}{\Delta x}$, where Δx is a representative time-averaged length scale. We approximate Δx by $C_1 D / N_{\text{cells}}$, where N_{cells} is the number of cells spanning the diameter of the droplet, and C_1 is some nondimensional constant. Introducing these steps into Eq. (24) yields,

$$\frac{dV}{dt} = - \left(\frac{6\mu_v N_{\text{cells}}}{\rho_l D^2 C_1} \right) V, \quad (25)$$

whose solution and associated droplet-center-of-mass displacement ($X - X_o$) can be obtained as

$$V = V_o \exp(-\kappa t), \quad \text{and} \quad (26)$$

$$\frac{X - X_o}{D} = \frac{V_o}{\kappa D} [1 - \exp(-\kappa t)]. \quad (27)$$

Here $\kappa = (6\mu_v N_{\text{cells}}) / (\rho_l D^2 C_1)$, and X_o denotes the position of the center of mass of the droplet at $t = 0$. Presenting this relation in terms of nondimensional time ($t^* = tV_o/D$), gives

$$\frac{X - X_o}{D} = \frac{1}{\tau} [1 - \exp(-\tau t^*)], \quad \text{where } \tau = \left(\frac{\mu_v}{\mu_L} \right) \frac{6N_{\text{cells}}}{\text{Re}_L C_1}. \quad (28)$$

In this particular case, with the size of the droplets being already so small, the effect of spatial resolution on the dynamics is particularly large. To illustrate this point, we consider the displacement as a function of time for both a 36 nm and a 36 μm diameter droplet. The results shown in Fig. 13 clearly demonstrate that the nanometer droplet is highly susceptible to grid resolution issues, which are not observed for the larger droplet.

One potential way to circumvent the dependency on numerical resolution is to employ an initially smooth velocity

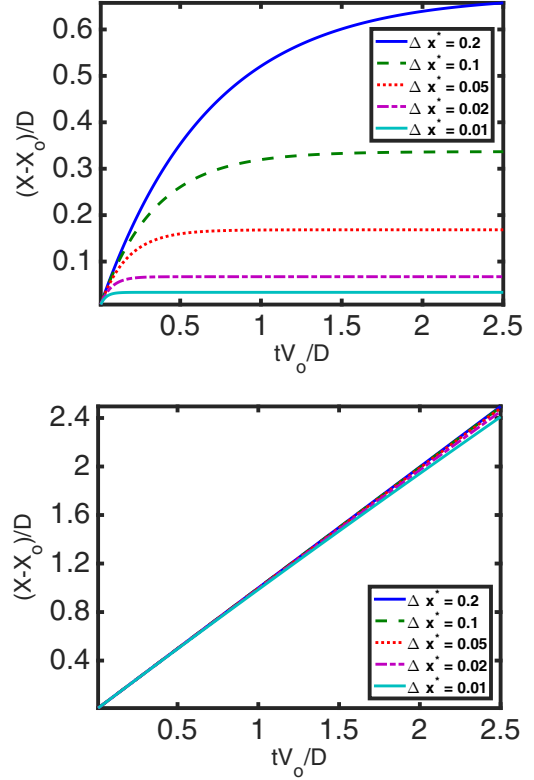


FIG. 13. Plot for analytical solution of displacement as a function of time and grid size for (a) nanometer ($D = 36\text{nm}$) and (b) micrometer-size droplet ($D = 36\mu\text{m}$).

profile, which decays from a magnitude of V_o in the liquid to zero in the gas phase over a distance much greater than Δx . In this manner, the issue of grid dependency on this initial profile will be absent, since the profile will be fully resolved at all grid levels. Due to the level of arbitrariness with the assumed mathematical form of this velocity profile, we have chosen not to follow this route, and to present the results based on the aforementioned initial velocity assignment. This is consistent with the standard practices in continuum-level simulations.

B. Molecular dynamics

With respect to the MD simulations, a potentially influential parameter is the time-step size. In order to study the sensitivity of results to Δt , the value is reduced from 0.006–0.003 ps with the remaining parameters kept constant as described in §III B. As shown in Fig. 14, the temporal evolution of kinetic energy for these simulations is essentially the same. It is observed that the energy drift for a 4500 ps long MD simulation is less than 10^{-4} of the initial total energy (E_{tot}) for $\Delta t = 0.006\text{ps}$ as compared with a value of 2×10^{-5} of E_{tot} for $\Delta t = 0.003\text{ps}$. These results indicate the MD simulation is converged with respect to time step size and that a value of $\Delta t = 0.006\text{ps}$ is sufficiently small to capture the system.

VI. A CLOSER LOOK AT THE NANOSCALE DROPLET COLLISION

In the first part of this section, we take a more detailed view of the comparison between MD and continuum droplet

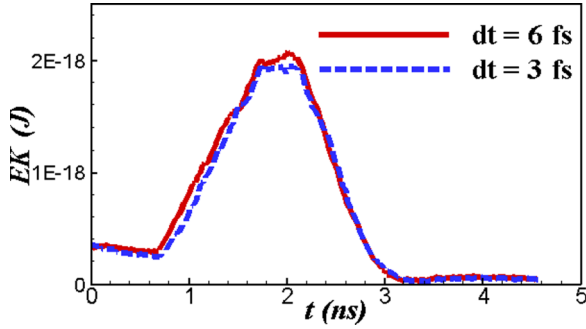


FIG. 14. The temporal evolutions of kinetic energy of liquid droplets during the collision from MD simulations with $dt = 0.006ps$ and $dt = 0.003ps$.

collision calculations presented previously in Sec. IV. This is followed by a comparison of collisions for pairs of droplets having different sizes, where the point of interest is the degree of departure from continuum behavior.

A. Similarities and differences between MD and continuum-level predictions

By considering the time histories of kinetic energy for both MD and continuum shown in Fig. 7 ($D = 36nm$), it is natural to consider two periods in the collision process. The first period corresponds to the preimpact phase and it is marked by the deceleration of droplets due to the increase of pressure between them and the action of viscous drag forces. The second period is characterized by the coalescence of the droplets.

Analysis in Sec. V A 3 shows that the level of numerical resolution of the velocity field, in particular the velocity gradient and its associated viscous drag component, plays a key role in the preimpact dynamics for continuum simulations. However, the differences between the MD and continuum results extend beyond the VoF numerical resolution of the velocity field. To gain a better appreciation of the difference, we consider the Knudsen number (Kn), as categorized by el Hak [44], namely

- (i) $Kn \leq 0.001$ (continuum),
- (ii) $0.001 < Kn \leq 0.1$ (slip-flow),
- (iii) $0.1 < Kn \leq 10$ [transition (moderately rarefied)], and
- (iv) $Kn > 10$ (free molecular flow).

In our particular case, for the gas phase we have from [44]

$$\lambda = \frac{k_B T}{\sqrt{2\pi} P \sigma^2} = 10.4nm \quad \text{and} \quad Kn_{\text{gas}} = \frac{\lambda}{L_g} = 1.972, \quad (29)$$

where k_B is Boltzmann constant, P_{sat} value is used for the value of pressure (P), and σ value is taken from Table IV. For liquid phase, using an estimate of lattice spacing as a substitute

TABLE IV. Physical properties of argon.

Parameters	Values
Molecular diameter, σ	0.341 nm
Molar volume of liquid, \bar{V}	$29.477 \times 10^{-6} m^3$

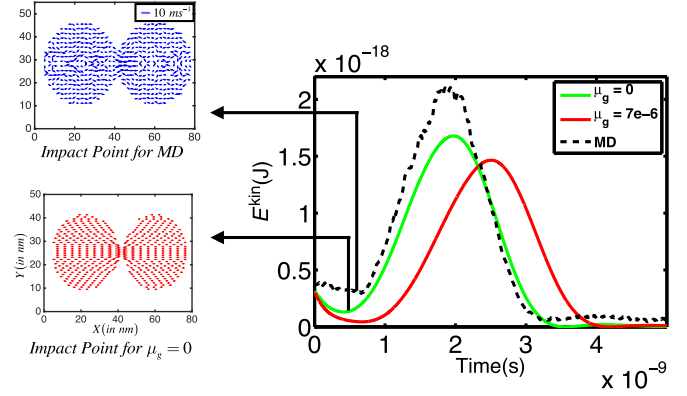


FIG. 15. Kinetic energy plot comparing continuum results with and without gas viscosity against MD simulations.

for mean-free path [6] the following values are obtained

$$\delta \sim \left(\frac{\bar{V}}{N_A} \right)^{1/3} = 0.36nm \quad \text{and} \quad Kn_{\text{liquid}} = \frac{\delta}{D} = 0.01. \quad (30)$$

The value of \bar{V} is taken from Table IV and N_A represents Avogadro's number. The corresponding Kn value puts the gaseous flow for this system in a moderately rarefied flow regime, while the liquid is in the slip-flow regime. While neither phase is expected to behave as a continuum, the deviation from continuum behavior is milder for the liquid phase due to its much lower value of Kn .

Consistent with this Kn characterization, the discrepancies observed in the preimpact period are not only caused by velocity field representation in VoF simulations as previously discussed, but also by the departure from continuum behavior. The interdroplet spacing, L_g , is simply too small to expect the Navier-Stokes to hold in this region. Similar observations have been presented in the literature (e.g., the work of Sirk [45]).

While viscous forces may contribute to the deviation occurring between MD and continuum calculations, the stress tensor (\mathbf{T}) solved in the Navier-Stokes also contains a pressure component [i.e., $\mathbf{T} = -P\mathbf{I} + \mu_g(\nabla\mathbf{u} + \nabla\mathbf{u}^T)$]. To see its effect in the collision process, the viscosity (μ_g) is set to zero and the calculation for the kinetic energy is repeated. The results, presented in Fig. 15, show a less pronounced reduction in kinetic energy when compared to the finite viscosity case. However, at earlier times during the preimpact phase the results are similar between both viscosity cases. Also, during this period both continuum calculations predict a kinetic energy that is substantially lower and decays in a qualitatively different manner compared to the MD results. This decay in kinetic energy is attributable to the stagnation pressure buildup in the interdroplet spacing region, which is specific to the continuum treatment. This trend is not observed in MD calculations. In fact in MD the kinetic energy decay is almost linear; it does not have the exponential decay observed in VoF simulations.

From Fig. 15, the postcollision stage begins at approximately 500 ps. Although the peak in kinetic energy is somewhat higher for the MD predictions, the trend in the kinetic energy rise and fall is strikingly similar between

both solution methods. The difference in peak kinetic energy between MD and VoF is, at least, partially attributable to the constrained no-slip flow during this period ($Kn_{\text{liquid}} = 0.01$).

An illustrative comparison between the distribution of velocities and the coalesced droplet shape evolution is shown in Fig. 16. The VoF calculation included in this figure corresponds to the zero viscosity case. From the initial impact (~ 500 ps) to the end of the collision process (~ 4400 ps), the results predicted by MD and VoF are quite alike. The initial ejection of liquid in the radial direction, i.e., normal to the preimpact droplet trajectory, is captured almost identically between both methods. Also the distribution and magnitude of velocities predicted by both methods agree well during the coalescence (~ 1000 ps to ~ 1900 ps), damped

oscillation (~ 2700 ps), and final decay of motion (~ 4400 ps). This behavior essentially means that once the droplets have coalesced and the dynamics are governed by the liquid phase, the notable differences between MD and continuum behavior diminished considerably. Again, making note of the respective Kn values, the corresponding liquid phase quantity is much closer to the continuum regime, and thus, this approximation to Navier-Stokes behavior is to some degree expected.

B. Size effect on droplet collision

Prediction of kinetic energy time histories for both MD and continuum level simulations are shown in Fig. 17 corresponding to droplets having a size of $D = 10\text{nm}$, 20nm ,

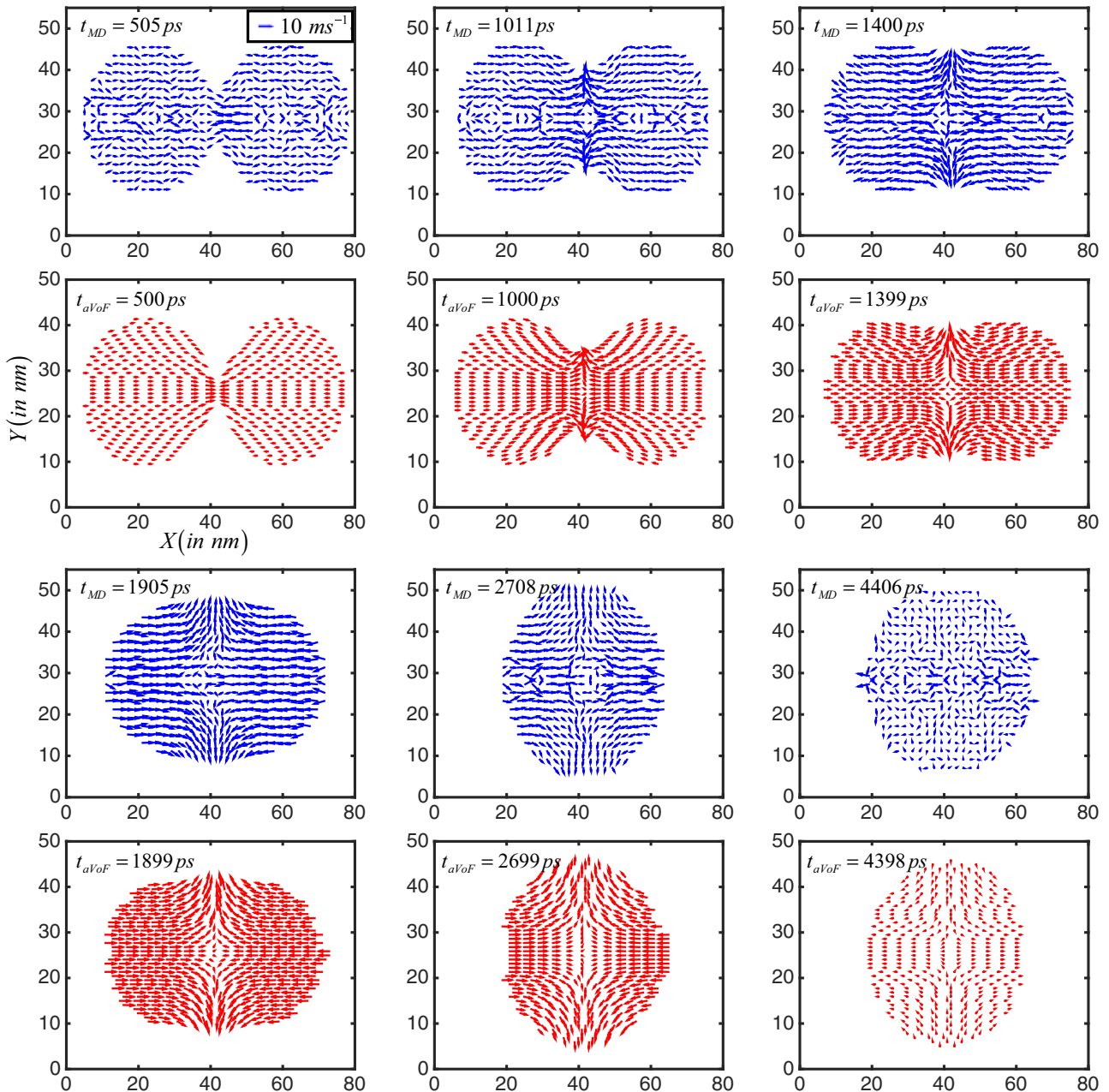


FIG. 16. Droplet images at various times during the collision process for $D = 36\text{nm}$. MD and VoF ($\mu_g = 0$) results are in blue and red, respectively. The images are captured along the center plane of the 3D domain.

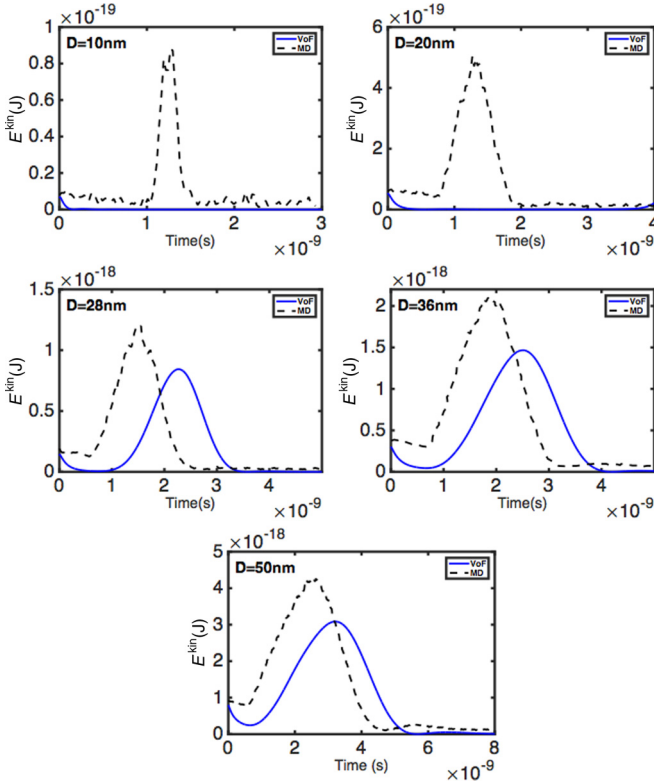


FIG. 17. Kinetic energy plots comparing continuum results with MD simulations for different diameters.

28nm, 36nm, and 50nm. In all of these calculations, the initial velocity of the droplets and interdroplet spacing remain the same as indicated in Table II. The time step and grid size used in VoF are respectively 1 ps and 1 nm.

Overall, the trend is one of increasing similarity between the two different sets of results as the droplet size increases. The most noticeable difference is the preimpact behavior. As shown in Table V, the Knudsen value for the gas remains the same as the benchmark case, and is thus within the moderately rarefied regime. With decreasing droplet size, the discrepancy between MD and continuum predictions become much more pronounced, as the time required for impact increases from $t_{\text{impact}} \sim 0.8$ ns for $D = 50$ nm to no impact observed for $D = 10$ nm. The reason behind this trend is explained by considering the ratio of droplet inertia to resistance forces, e.g., viscous and pressure buildup. This is equivalent to the Reynolds number, which shrinks with decreasing D . Hence, for a critical value of the Reynolds number, the resistance forces will be such that they will completely impede droplet contact.

TABLE V. Knudsen number values for all droplet collision cases.

Droplet diameter (D)	$\text{Kn}_{\text{gas}} = \lambda/L_g$	$\text{Kn}_{\text{liquid}} = \delta/D$
10 nm	1.972	0.036
20 nm	1.972	0.018
28 nm	1.972	0.013
36 nm	1.972	0.01
50 nm	1.972	0.0072

With respect to the liquid phase dynamics, the Knudsen numbers vary as indicated in Table V; however, they remain within the slip-flow regime. Provided the droplets are sufficiently large to produce impact, the results show that the relative magnitude for the peak in kinetic energy, between MD and continuum simulations, increases with decreasing droplet size. However, it is the preimpact period that exhibits the strongest departure from continuum behavior.

VII. CONCLUSIONS

The current work presents a direct comparison between molecular dynamics and continuum-level (Navier-Stokes with volume-of-fluid) simulations of binary droplet collision for nanometer-sized argon droplets. The results show that both methodologies predict reasonably similar behavior as the droplet diameter approaches 50 nm. At the other extreme, for droplets having diameters at or below 10 nm, the trends, characterized by kinetic energy time histories, show markedly different behavior.

A prominent aspect of the MD-continuum difference occurs during the trajectory of the droplets through the gas phase before any contact has been established. During this preimpact period, continuum simulations largely overpredict the degree of resistance, contributed by both viscous and pressure effects, resulting in a strong decline in the kinetic energy, and consequently a longer time for contact to occur. In fact, for sufficiently small droplets ($D < 28$ nm), this impact never occurs. Due to the large value for the Knudsen number corresponding to droplet-gas interactions ($\text{Kn}_{\text{gas}} = 1.972$), this behavior is expected. Conversely, once the droplets have made contact, the surface tension forces immediately act to produce coalescence with little to no secondary oscillations. This postimpact period sees good agreement between MD and continuum simulations. The liquid-based Knudsen number ranges between 0.036 and 0.0072 for respective droplet diameters between 10 nm and 50 nm, and thus the dynamics are expected to be much closer to the continuum behavior than the corresponding preimpact period.

The conclusions from this work can be extended to systems of nanodroplets. If the droplets are smaller than 50 nm, it is expected that some degree of departure from continuum-based behavior will result for the prediction of movement of these droplets within the gas phase. In fact, it is this motion where the deviations from continuum behavior are the strongest. Thus, for a cloud of nanodroplets where their size is significantly below the 50 nm mark, it is envisioned that the droplet transport will significantly depart from continuum behavior. Once collisions have occurred, however, the similarities with continuum behavior are strong.

ACKNOWLEDGMENTS

We would like to thank eXtreme Science and Engineering Discovery Environment (XSEDE) for providing the RPI group supercomputer resources for MD simulations. Additionally, the RPI authors are grateful for the support provided by the New York State NYSTAR funded Focus Interconnect Center at their institution. UW-Madison authors would like to acknowledge the support of the Office of Naval Research

under code 331, and the CBET Thermal Transport Processes program of the National Science Foundation. CEI is also ac-

knowledged for granting use of their postprocessing software, ENSIGHT.

-
- [1] K. P. Travis, B. D. Todd, and D. J. Evans, *Phys. Rev. E* **55**, 4288 (1997).
- [2] C. Liu and Z. Li, *AIP Advances* **1**, 032108 (2011).
- [3] M. Gărăjeu, H. Gouin, and G. Saccomandi, *Phys. Fluids* **25**, 082003 (2013).
- [4] J. Pfahler, J. Harley, H. Bau, and J. Zemel, *Sensors and Actuators A: Physical* **22**, 431 (1990).
- [5] M. L. Gee, P. M. McGuiggan, J. N. Israelachvili, and A. M. Homola, *J. Chem. Phys.* **93**, 1895 (1990).
- [6] K. V. Sharp, R. J. Adrian, J. G. Santiago, and J. I. Molho, in *The MEMS Handbook*, edited by M. G. el Hak (CRC Press, Boca Raton, 2001), Chap. 10.
- [7] J. B. Boreyko and C.-H. Chen, *Phys. Rev. Lett.* **103**, 184501 (2009).
- [8] C. Lv, P. Hao, Z. Yao, Y. Song, X. Zhang, and F. He, *Appl. Phys. Lett.* **103**, 021601 (2013).
- [9] Y. Nam, H. Kim, and S. Shin, *Appl. Phys. Lett.* **103**, 161601 (2013).
- [10] R. Enright, N. Miljkovic, J. Sprittles, K. Nolan, R. Mitchell, and E. N. Wang, *ACS Nano* **8**, 10352 (2014).
- [11] N. Miljkovic, R. Enright, Y. Nam, K. Lopez, J. Sack, and E. N. Wang, *Nano Lett.* **13**, 179 (2013).
- [12] J. B. Boreyko, Y. Zhao, and C.-H. Chen, *Appl. Phys. Lett.* **99**, 234105 (2011).
- [13] K. M. Wisdom, J. A. Watson, X. Qu, F. Liu, G. S. Watson, and C.-H. Chen, *Proc. Natl. Acad. Sci. USA* **110**, 7992 (2013).
- [14] N. Miljkovic, D. J. Preston, R. Enright, and E. N. Wang, *Appl. Phys. Lett.* **105**, 013111 (2014).
- [15] M. Kalweit and D. Drikakis, *Phys. Rev. B* **74**, 235415 (2006).
- [16] K. Willis and M. Orme, *Exp. Fluids* **34**, 28 (2003).
- [17] Y. Pan and K. Suga, *Phys. Fluids* **17**, 082105 (2005).
- [18] N. Nikolopoulos, K.-S. Nikas, and G. Bergeles, *Comput. Fluids* **38**, 1191 (2009).
- [19] P. R. Brazier-Smith, S. G. Jennings, and J. Latham, *Proc. R. Soc. London A* **326**, 393 (1972).
- [20] J. Qian and C. K. Law, *J. Fluid Mech.* **331**, 59 (1997).
- [21] L. Ming, N. Marković, M. Svanberg, and J. B. C. Pettersson, *J. Phys. Chem. A* **101**, 4011 (1997).
- [22] I. Chun, M. Y. Ha, J. Jang, and H. S. Yoon, *Bulletin of the Korean Chemical Society* **32**, 2027 (2011).
- [23] S. Kim, *J. Korean Phys. Soc.* **57**, 1339 (2010).
- [24] J.-C. Pothier and L. J. Lewis, *Phys. Rev. B* **85**, 115447 (2012).
- [25] J. Koplik, S. Pal, and J. R. Banavar, *Phys. Rev. E* **65**, 021504 (2002).
- [26] S. S. Deshpande, L. Anumolu, and M. F. Trujillo, *Comput. Sci. Discovery* **5**, 014016 (2012).
- [27] J. U. Brackbill, D. B. Kothe, and C. Zemach, *J. Comput. Phys.* **100**, 335 (1992).
- [28] R. I. Issa, *J. Comput. Phys.* **62**, 40 (1986).
- [29] D. Enright, R. Fedkiw, J. Ferziger, and I. Mitchell, *J. Comput. Phys.* **183**, 83 (2002).
- [30] Z. Wang, J. Yang, B. Koo, and F. Stern, *Int. J. Multiphase Flow* **35**, 227 (2009).
- [31] M. Sussman and E. G. Puckett, *J. Comput. Phys.* **162**, 301 (2000).
- [32] J. J. E. Pilliod and E. G. Puckett, *J. Comput. Phys.* **199**, 465 (2004).
- [33] F. Xiao, S. Ii, and C. Chen, *J. Comput. Phys.* **230**, 7086 (2011).
- [34] G. C. Maitland, M. Rigby, E. B. Smith, and W. A. Wakeham, *Phys. Today* **36**, 57 (1983).
- [35] D. Frenkel and B. Smit, *Understanding molecular simulation: From algorithms to applications*, (Academic Press, Cambridge, Massachusetts, 2002), p. 75.
- [36] H. J. C. Berendsen, J. P. M. Postma, W. F. V. Gunsteren, A. D. Nola, and J. R. Haak, *J. Chem. Phys.* **81**, 3684 (1984).
- [37] J. Walton, D. Tildesley, J. Rowlinson, and J. Henderson, *Mol. Phys.* **48**, 1357 (1983).
- [38] J. G. Kirkwood and F. P. Buff, *J. Chem. Phys.* **17**, 338 (1949).
- [39] M. Allen and D. Tildesley, *Computer simulation of liquids*, (Clarendon Press, Oxford, 2000), Chap. 2.
- [40] Z. Liang and P. Keblinski, *Appl. Phys. Lett.* **107**, 143105 (2015).
- [41] C. Galusinski and P. Vigneaux, *J. Comput. Phys.* **227**, 6140 (2008).
- [42] F. F. Abraham, *Phys. Fluids* **13**, 2194 (1970).
- [43] R. Clift, J. R. Grace, and M. E. Weber, *Bubbles, Drops, and Particles* (Academic Press, Cambridge, Massachusetts, 1978).
- [44] M. G. el Hak, *J. Fluids Eng.* **121**, 5 (1999).
- [45] T. Sirk, Numerical simulation of nanoscale flow: A molecular dynamics study of drag, Master's Thesis, Virginia Polytechnic Institute and State University, 2006 (unpublished).